Journal of Metamorphic Geology

WILEY

Journal of METAMORPHIC GEOLOGY

ORIGINAL ARTICLE OPEN ACCESS

Experimental Replacement of Zircon by Melt-Mediated Coupled Dissolution-Precipitation Causes Dispersion in U–Pb Ages

Jeremy L. Asimus[1] | Nathan R. Daczko[2] | Jean-Antoine Gazi[2] | Isra S. Ezad[2,3] | Ivan Belousov[4] | Thomas Rodemann[5] | Jacqueline A. Halpin[1,6] | Sandra Piazolo[7]

[1]Institute for Marine and Antarctic Studies, University of Tasmania, Hobart, Australia | [2]ARC Centre of Excellence for Core to Crust Fluid Systems and GEMOC, School of Natural Sciences, Macquarie University, Sydney, Australia | [3]Centre for Exploration Targeting, School of Earth Sciences, University of Western Australia, Perth, Australia | [4]Centre for ore Deposit and Earth Sciences (CODES), University of Tasmania, Hobart, Australia | [5]Central Science Laboratory (CSL), University of Tasmania, Hobart, Australia | [6]The Australian Centre for Excellence in Antarctic Science, University of Tasmania, Hobart, Australia | [7]School of Earth and Environment, University of Leeds, Leeds, UK

Correspondence: Jeremy L. Asimus (jeremy.asimus@utas.edu.au)

Received: 7 March 2024 | **Revised:** 24 July 2024 | **Accepted:** 2 August 2024

Funding: This study was financially supported internally through the School of Natural Sciences, Macquarie University, and by the Geological Society of Australia, through the GSA endowment fund.

Keywords: coupled dissolution-precipitation | experimental petrology | melts | U–Th–Pb | zircon

ABSTRACT

Zircon geochronology provides critical information on the rates and durations of geological processes and enables researchers to explore deep time. However, some zircon datasets show a continuum of concordant ages ('smear') without well-defined age populations. These age smears are typically interpreted to represent variable loss of radiogenic Pb or protracted geological events lasting tens of millions of years. Coupled dissolution-precipitation replacement of zircon has been suggested as one process that may produce these complex age datasets. Here, we react fragments of the well characterised Mud Tank zircon standard with natural intermediate and mafic melts (0.9 GPa, 1100–1180°C) to test if short-term exposure to a melt can modify the geochronological patterns of zircon. Our observations show that within a short duration (18 h to 3.5 days), most Mud Tank zircon fragments display microstructural and/or chemical evidence for modification by dissolution at fragment boundaries along with partial replacement by coupled dissolution-precipitation processes. The replaced zircon domains have U–Pb ages that smear over one hundred million years, between 764–647 Ma, illustrating variable mobility and redistribution of the U and Pb isotopes. Our experiments demonstrate that zircon modified by coupled dissolution-precipitation replacement may not faithfully record the age or duration of geological events and that investigation of zircon microstructure in high-resolution backscattered electron, cathodoluminescence imaging and/or Raman mapping is needed to better understand complex zircon geochronological datasets.

1 | Introduction

Zircon ($ZrSiO_4$) is a commonly occurring accessory mineral known for its high uranium (U) concentrations relative to its host rock, whilst lead (Pb) is inherently incompatible and does not integrate into the crystal structure during crystallisation. The remarkable resilience of zircon through high-grade metamorphism and crustal melting events enables it to preserve its isotopic signature, including U and accumulated radiogenic Pb (Cherniak and Watson 2001; Moller et al. 2003). Zircon also

incorporates trace elements such as hafnium (Hf), rare earth elements (REE), yttrium (Y), and titanium (Ti), offering valuable insights into the crustal provenance and the magmatic or metamorphic history of the rocks from which it originated (e.g., Belousova et al. 2002; Hawkesworth and Kemp 2006; Simon, Kelly, and Moller 2007). The oxygen isotope composition of zircon can identify the contributions of various mantle and crustal sources to the host magma (e.g., Valley 2003). Meanwhile, uranium-thorium-helium (U–Th–He) thermo-chronometry aids in determining rates of crustal exhumation and landscape development (e.g., Reiners 2005). Linking zircon age and chemistry has established its use as a robust mineral geochronometer, providing crucial information for understanding the history of Earth, including Early Earth evolution, the development of oceans, continental amalgamation and dispersal, rates of mountain-building events, and the timescales of magmatic and volcanic processes (e.g., Belousova et al. 2002; Charlier et al. 2005; Scherer, Whitehouse, and Munker 2007).

For U–Pb dating, zircon ideally exhibits one of two behaviours. In the first scenario, the zircon behaves as a closed system, unaffected by external factors, resulting in a Gaussian distribution of concordant apparent ages that represent the crystallisation age. In the second scenario, zircon grains are disturbed by a 'Pb-loss event' producing ages that form a single discordant array. The upper intercept of the array represents the crystallisation age of the zircon, whereas the lower intercept represents the age of the Pb-loss event. However, many rock samples fall into non-ideal scenarios where zircon age patterns comprise a mix of concordant and discordant data, scattered along and near the concordia. In these complex cases, zircon grains show evidence of Pb-loss, addition of common Pb, redistribution and clustering of Pb within a grain and possibly the mobilisation of U (e.g., Halpin et al. 2020; Rimša et al. 2007; Spier, Filho, and Daczko 2022; Spier, Daczko, and Zhou 2024; Taylor et al. 2023). Processes like crystal plastic deformation (Piazolo, Austrheim, and Whitehouse 2012), metamict zircon diffusion (Cherniak and Watson 2001) and fluid-mediated replacement of zircon by coupled dissolution-precipitation replacement (Geisler, Schaltegger, and Tomaschek 2007; Kelly et al. 2017), sometimes referred to as interface-coupled dissolution-precipitation (Fougerouse et al. 2024; Vonlanthen et al. 2012) or coupled dissolution-reprecipitation (e.g., Altree-Williams et al. 2015), can facilitate mobilisation and redistribution of trace elements, resulting in complex zircon datasets with variable U–Pb spot ages and trace element chemistry. In such cases, deriving meaningful geological information from zircon chemistry is challenging and requires an in-depth understanding of the processes that have led to trace element mobilisation.

Experimental studies on Pb mobility in zircon have explored solid-state thermal diffusion and fluid-mediated dissolution-precipitation processes. Solid-state diffusion proves inefficient, even at temperatures of ~1000°C, unless zircon grains have accumulated significant radiation damage (Cherniak and Watson 2001, 2003). Conversely, experiments with alkali- and F-bearing fluids demonstrate near-total radiogenic Pb loss from zircon under various temperature and pressure conditions, emphasising the importance of fluid-mediated alteration (Geisler et al. 2003; Harlov, Anczkiewicz, and Dunkley 2023; Lenting et al. 2010; Lewerentz et al. 2019; Wang et al. 2024). However, there are no studies in which zircon is experimentally altered in the presence of common silicate melts despite increasing recognition of melt-mediated coupled dissolution-precipitation replacement reactions causing complex U–Pb age arrays, trace element patterns and Hf isotopic compositions in natural zircon (Halpin et al. 2020; Spier, Filho, and Daczko 2022; Spier, Daczko, and Zhou 2024; Wang et al. 2024).

Coupled dissolution-precipitation replacement, a fluid-mediated mineral replacement reaction process (Putnis 2009), plays an under-recognised role in modifying zircon. For a comprehensive review of coupled dissolution-precipitation see Putnis (2009) and Ruiz-Agudo, Putnis, and Putnis (2014). In short, this mechanism involves the dissolution of a primary mineral when exposed to a reactive fluid, which locally changes the composition of the boundary fluid and triggers precipitation of a secondary mineral of a different composition at the interface, though this can be the same mineral species. The presence of fluid-filled porosity within the product phase is a necessary characteristic of coupled dissolution-precipitation replacement, as porosity allows the fluid to reach the reaction interface (Putnis and John 2010). The reaction interface can then propagate inwards, supplying the necessary fluid to advance further replacement of the precursor mineral (Putnis and John 2010). After replacement, the porosity may be filled with secondary minerals (e.g., Harlov, Wirth, and Förster 2005). In both nature and experiments the interface between original and replaced minerals are commonly characterised by irregular boundaries and embayments (Koehn et al. 2021 and references therein).

Coupled dissolution-precipitation replacement of zircon has been recognised in many rock types from a range of tectonic environments through time, spanning sites of Archean magmatism (e.g., Spier, Filho, and Daczko 2022; Spier, Daczko, and Zhou 2024) through to modern mid-ocean ridge (e.g., Schwartz et al., 2022). Melt-mediated coupled dissolution-precipitation replacement of zircon has been recognised in natural magmatic systems such as granites (Halpin et al. 2020) and layered mafic intrusions (Spier, Filho, and Daczko 2022; Spier, Daczko, and Zhou 2024), as well as high grade melt-bearing metamorphic rocks (Laurent et al. 2018; Wang et al. 2024), that in some cases are overprinted by hydrothermal fluid–rock interaction (Kelly et al. 2017; Vonlanthen et al. 2012). In zircon, the characteristic microstructural features that have been linked to melt-mediated coupled dissolution-precipitation include rounded grain terminations, modified and blurred growth zonation, pore formation, and the development of an abundance of mineral inclusions (Figure 1; Geisler, Schaltegger, and Tomaschek 2007). Representative examples of these features that serve as indicators of zircon modification by coupled dissolution-precipitation replacement are highlighted in Figure 1 and focus attention on the geological significance of the related complex U–Pb age arrays, trace element patterns and Hf isotopic compositions in the modified zircon examined in those studies.

Here, we present results from a series of novel melt-zircon interaction experiments using the Mud Tank zircon U–Pb age standard (Gain et al. 2019). Experiments were run with melts of Zr undersaturated intermediate and mafic composition as the reactive fluid at temperatures of 1100°C and 1180°C for durations between 18 h

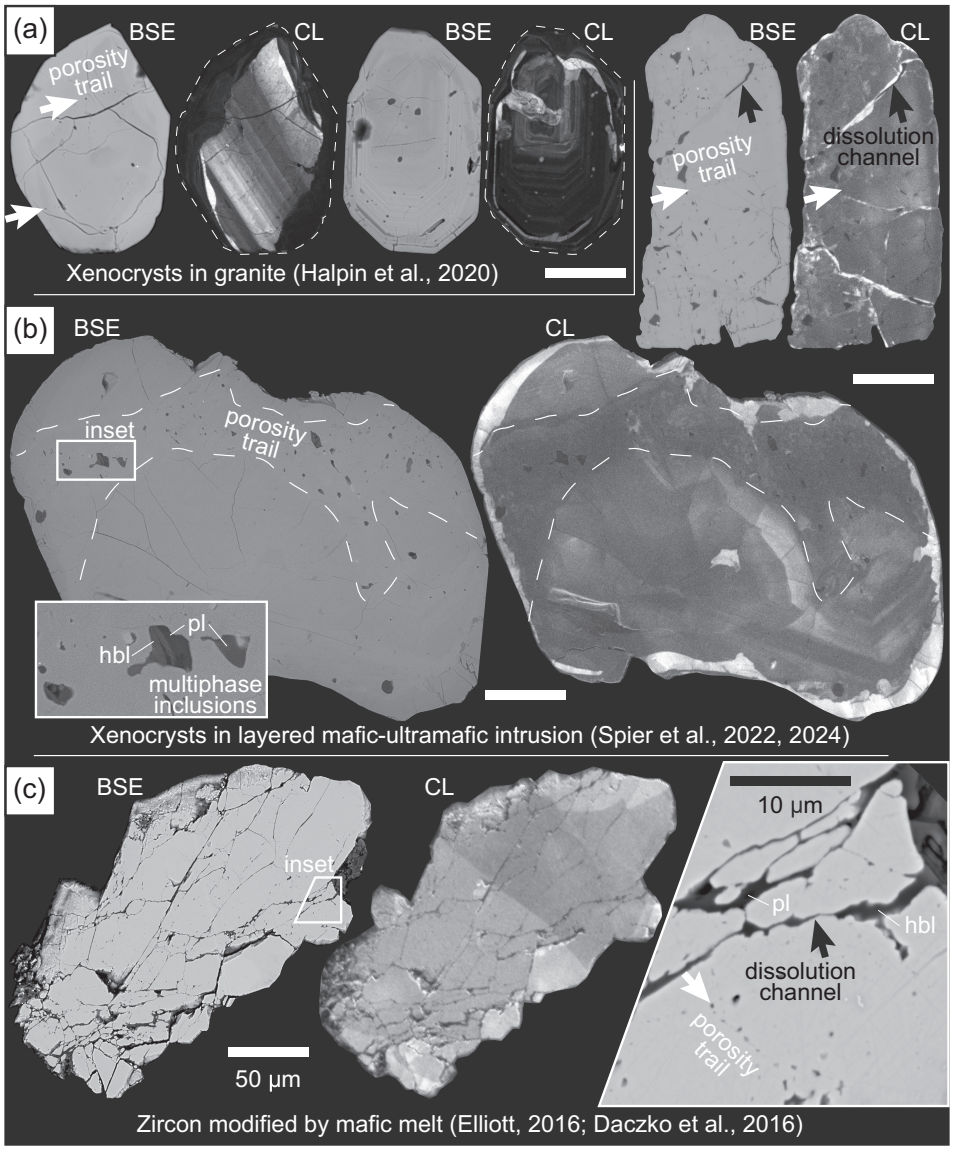

FIGURE 1 | Backscattered electron (BSE) and cathodoluminescence (CL) images of natural zircon coupled dissolution-precipitation replacement textures: (a) zircon xenocrysts in a granite from the Bruce Rise, Antarctica (Halpin et al. 2020), (b) zircon xenocrysts in layered mafic-ultramafic intrusions from the Guyana Shield, Brazil (Spier, Filho, and Daczko 2022; Spier, Daczko, and Zhou 2024) and (c) zircon modified by mafic melts migrating through a high strain zone, New Zealand (Elliot 2016; Daczko et al. 2016). Key textures include porosity trails (white arrows), dissolution channels (black arrows), mineral inclusions (with minerals labelled) and truncated, convolute and modified cathodoluminescence responses. All scale bars are 50 µm.

and 3.5 days. The microstructural, chemical, and isotopic composition of the reaction products were characterised using backscattered electron (BSE) and cathodoluminescence (CL) imaging, Raman mapping and U–Pb and trace element LA-ICPMS analysis.

2 | Methods

2.1 | Experimental Setup

Melt-zircon reaction experiments were performed using a rapid quench piston cylinder apparatus with a standard ½″ CaF_2 cell assembly (Figure 2; Asimus, Daczko, and Ezad 2023; Ezad et al. 2023). The assembly includes a MgO inner sleeve, a graphite furnace, CaF_2 outer sleeves and type B Pt-Rh thermocouple wires (Figure 2). No friction correction was applied to the CaF_2 assemblies. Two different melt compositions (intermediate and mafic) were used in the experiments to investigate the effect of melt composition on melt-zircon reactions. To create an intermediate melt, we used a sample of the Mawson Charnockite, Antarctica, with SiO_2, MgO and total alkali (Na_2O and K_2O) contents of 64.3 wt%, 2.02 wt% and 6.16 wt%, respectively (Data S1; LM53 in Halpin et al. 2012). For a mafic melt, we used a homogenous diorite gneiss from the Western Fiordland Orthogneiss, New Zealand, with SiO_2, MgO and total alkali compositions of 54.85 wt%, 4.4 wt% and 5.64 wt%, respectively (Data S1; LG4050 in Daczko and Halpin 2009).

To ensure Zr undersaturation and thus reactivity, zircon grains were removed from the crushed charnockite (Zr = 342 ppm;

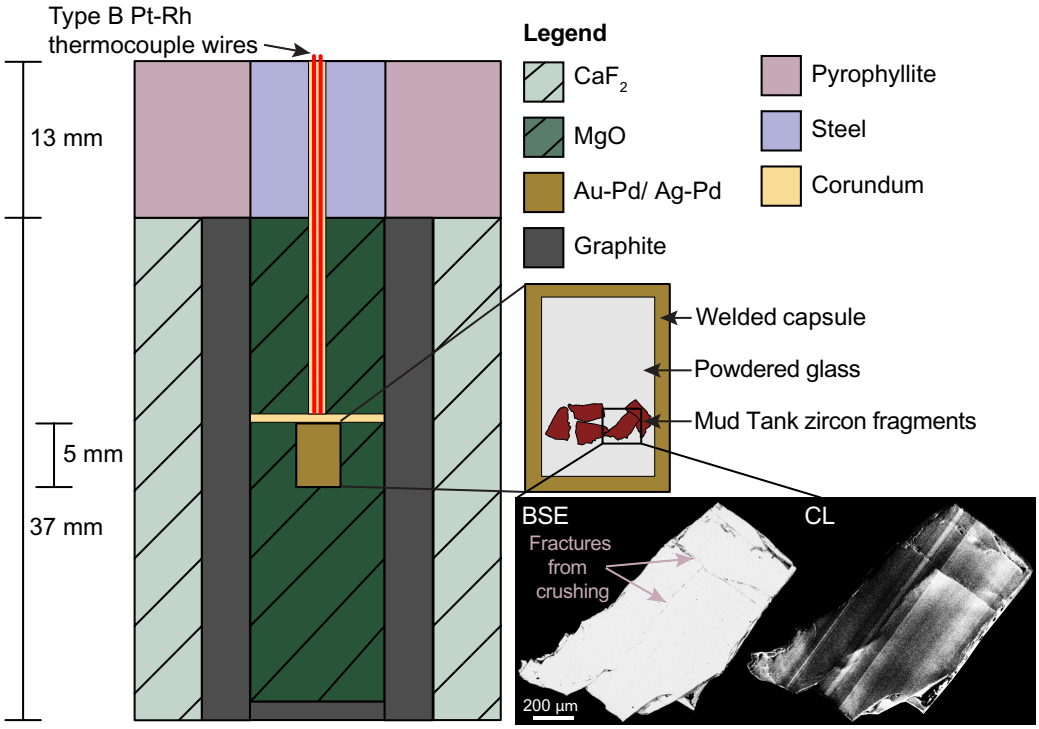

FIGURE 2 | Piston cylinder cell design used in the melt-zircon reaction experiments. Powdered mafic or intermediate glass and crushed Mud Tank zircon fragments were encased in approximately 3 × 5 mm, welded Au–Pd or Ag–Pd capsules. The capsule was placed within a standard ½″ CaF_2 cell assembly (Asimus, Daczko, and Ezad 2023; Ezad et al. 2023). Experiments were run at high temperature crustal conditions for variable durations to investigate melt-zircon reactions.

TABLE 1 | Experimental conditions of melt glassing and melt-zircon reaction experiments.

Experiment ID	Experiment type	Melt composition	Capsule material	Pressure (kbar)	Temperature (°C)	Run time (days)
GL-1	Glassing	Intermediate	Au–Pd	10.5	1100	0.25
MO-21-42	Glassing	Mafic	Au–Pd	10.5	1250	0.25
MO-21-48	Glassing	Mafic	Ag–Pd	10.5	1200	0.25
A-21-08	Glassing	Mafic	Au–Pd	10.5	1250	0.25
MO-20-21	Reaction	Intermediate	Au–Pd	9	1100	0.75
MO-21-43	Reaction	Mafic	Au–Pd	9	1180	1
MO-21-47	Reaction	Mafic	Ag–Pd	9	1180	3.5

Note: The starting composition of the mafic melts was a homogeneous diorite gneiss from the Western Fiorldland Orthogneiss, New Zealand (LG4050; Daczko and Halpin 2009), whereas the felsic melt was created from a sample of Mawson Charnockite, Antarctica (LM53; Halpin et al. 2012). Geochemical compositions of the glass are available in Table S1. Ag–Pd capsules were used due to a lack of availability of Au–Pd.

Data S1) using conventional heavy liquid and magnetic separation techniques. The remaining sample was milled into a powder. The powder was melted and quenched in a precursor experiment to homogenise the composition of the starting melt (GL-1; Table 1) for the melt-zircon reaction experiments. No zircon separation was performed for the dioritic gneiss (Zr = 42 ppm; Data S1), which was milled into a powder, melted and quenched in multiple precursor experiments (MO-21-42, MO-21-48 and A-21-08; Table 1). The glasses were finely ground using a mortar and pestle and combined with crushed fragments of Mud Tank zircon (Gain et al. 2019) in Au–Pd or Ag–Pd capsules. We present three melt-zircon reaction experiments that were performed at high-temperature crustal conditions for variable durations to capture the development of melt-mediated coupled dissolution precipitation replacement in zircon (Table 1): MO-20-21 (intermediate melt, 9 kbar, 1100°C, 18 h), MO-21-43 (mafic melt, 9 kbar, 1180°C, 24 h) and MO-21-47 (mafic melt, 9 kbar, 1180°C, 3.5 days). A regular decompression procedure was used for experiment MO-21-43 (Table 1). To reduce decompression cracking in the subsequent experiments, a slow decompression (12 h) procedure was used for MO-20-21 and MO-21-47.

2.2 | Backscattered Electron, Cathodoluminescence and Raman Imaging

The experiment capsules were mounted in epoxy and then polished until a surface with zircon was exposed. The microstructure of zircon was imaged using a FEI Teneo Field Emission Scanning Electron Microscope (FEI-SEM) at Macquarie University GeoAnalytical (MQGA), Sydney. Backscatter electron imaging was performed using a 12 mm working distance, 15 kV accelerating voltage and 5 μs dwell time. Cathodoluminescence (CL) imaging of zircon fragments within the experiments was conducted by a Zeiss EVO MA15 scanning electron microscope at MQGA, with operating conditions of a 12 mm working distance and 25 kV accelerating voltage.

Zircon grains within the melt-zircon reaction experiments were analysed with a Renishaw inVia Streamline Raman microscope at the Central Science Laboratory (CSL), University of Tasmania. The Renishaw inVia Streamline Raman microscope is equipped with a 532 nm laser and operated at 22 mW using a 100× (NA 0.9) objective and a 0.005 s exposure. The spectra were recorded with a 2400 I/mm grating resulting in a spectral resolution of 1.75 cm^{-1}. The areas were mapped using a 0.5 μm step size in x and y, matching the expected laser spot of ~0.5 μm. The BSE, CL and Raman imaging were used to distinguish between unmodified and replaced domains within the zircon to target for U–Pb dating.

2.3 | Electron Microprobe Analysis

The composition of the glass was measured using an electron microprobe for major elements (Data S1) as phenocrysts were identified in the matrix of the melt-zircon reaction experiments and likely crystallised during the experiments, modifying the original composition of the melt (Figures 3–5). Compositional analyses were performed on a JEOL JXA-8530F Plus field emission electron microprobe equipped with 5 wavelength dispersive spectrometers at an accelerating voltage of 15 keV, beam current of 20 nA and beam diameter of 10 μm at CSL, University of Tasmania. The standards used for calibration include:USGS basaltic glass BCR-2G for Si, Al, Fe, Mg, Ca, Na, K, synthetic rutile for Ti, natural fluoro-apatite for P and rhodonite for Mn (all P&H Developments, UK). The peak counting time was 30 s for Mg, Al, Ti and Mn and 20 s for all other elements. The background correction method was linear for K, exponential for Mg, P, Ti, Mn, and mean atomic number for Si, Al, Fe, Ca and Na. The background counting time was 10 s for K, 20 s for P, and 30 s for Mg, Ti and Mn. The PAP matrix correction procedure was used. Na, K, Si, Ca and Fe were measured first on their respective spectrometers, and intensities were monitored for time-dependent intensity loss or gain.

2.4 | LA-ICPMS U–Pb Ages and Trace Elements

U–Pb and trace element analyses of zircon fragments and glass in the melt-zircon reaction experiments were performed with an ASI RESOLution S-155 ablation system with Coherent Compex Pro 110 Ar-F excimer laser operating at a 193 nm wavelength and a pulse width of 20 ns at CODES Analytical Laboratories, University of Tasmania. The laser system was coupled to an Agilent 7900 quadrupole ICP-MS. The zircon fragments were analysed using a 20 μm spot size, whereas the glass was analysed using a 30 μm spot size. Spot locations are provided in Data S2. Other analytical conditions are described in Data S3 and Thompson, Meffre, and Danyushevsky (2018).

The data reduction used for zircon U–Pb dating was based on the method outlined in detail in Thompson, Meffre, and Danyushevsky (2018) and Halpin et al. (2014) and was performed in LADR (Norris and Danyushevsky 2018). Time-resolved $^{206}Pb/^{238}U$ signal traces and trace element concentrations were examined on a Concordia diagram to select the most representative age. A single signal selection >10 s was made for most zircon spot analyses ($n = 70$) that display relatively constant $^{206}Pb/^{238}U$ and trace element concentrations (e.g., La) across the signal (Data S4). In three zircon spot analyses with variable trace element concentration, the signal was divided into two sections of higher and lower trace element concentrations ($n = 6$). The divided signals were >10 s and have uniform $^{206}Pb/^{238}U$ signals. The U–Pb isotopic character of the glass was selected from spot analyses with signals >20 s that displayed uniform trace element concentrations ($n = 20$) (Data S4).

The downhole fractionation, instrument drift and mass bias correction factors for Pb/U ratios were calculated using analyses of the 91,500 standard (Wiedenbeck et al. 1995). The instrument drift and mass bias correction factors for the $^{207}Pb/^{206}Pb$ ratio and $^{207}Pb/^{206}Pb$-based ages were calculated using analyses of the NIST610 glass, using the Pb isotopic values of Baker et al. (2004). The calibration of the U–Pb ages was checked on analyses of the Temora zircon (Black et al. 2004) and the Plešovice zircon (Sláma et al. 2008), which were analysed throughout the analytical session and treated as unknowns as an independent control of accuracy and precision. The primary zircon standard 91,500 yields a weighted mean $^{206}Pb/^{238}U$ age of 1063.48 ± 1.38 Ma (MSWD = 0.93, $n = 34$), which is within error of the recommended value of 1062.4 ± 0.4 Ma (Wiedenbeck et al. 1995). The weighted mean $^{206}Pb/^{238}U$ ages for the secondary standards Temora and Plešovice (at 95% confidence) are 414.47 ± 2.03 Ma (MSWD = 2.5, $n = 15$) and 338.16 ± 1.43 Ma (MSWD = 1.2, $n = 14$), respectively. These are within the published TIMS zircon ages of 416.8 ± 1.1 Ma for Temora (Black et al. 2004) and 337.13 ± 0.37 Ma for Plešovice (Sláma et al. 2008).

Trace element abundances in zircon were calibrated on the NIST610 glass using values of Jochum et al. (2011), using secondary standard corrections based on the compositions of glasses BCR-2G and GSD-1G (GeoReM preferred values; http://georem.mpch-mainz.gwdg.de/). Quantification was performed using ^{91}Zr as the internal standard element, normalising all measured cations to the Zr site total of a stoichiometric zircon. The 91,500 zircon and the NIST610, BCR-2G and GSD-1G glasses were analysed in duplicate at the beginning, end, and every 60 min throughout the analytical session. Trace element abundances measured in the 91,500 zircon are in the range of reported values from the GeoReM website. As some ablation volumes of the zircon fragments included small proportions of glass that are visible in the BSE images, the trace element data is used to estimate the percentage of zircon and glass for each analysis (see Data S4 for calculations).

3 | Results

3.1 | Microstructures and Raman Mapping of Zircon

Across all experiments, the crushed zircon fragments ('grains') are typically elongate and angular, with smoothly curved fracture surfaces ('grain boundaries') and gently rounded corners (Figures 3e, 4b and 5f). Two types of fractures transgress the experiments. One type are decompression fractures that appear black in BSE images and are continuous through zircon and glass ('decompression fracture', Figures 3a and 5b). The other type are glass-filled fractures that only transgress zircon fragments and are grey in BSE images ('glass-filled fracture', Figures 3–5).

Fragments contain very small (<1 μm) glass-filled circular to triangular pores, as well as highly elongate, variably thick, glass-filled discontinuous channels (black arrows, Figures 3b–d, 4c–f and 5e–g). Pores occur in domains or form discontinuous trails of variable length. No mineral inclusions were identified within the glass filled pores. Some fragments only in the mafic melt-zircon reaction experiments show domains with many narrow (<20 μm) channels that surround islands of zircon ('islands', Figures 3a and 4a). These channels comprise up to 7% surface area of the zircon domains. Highly rounded and cuspate shapes characterise the islands and some have short segments with straight grain boundaries (red lines in Figures 3e and 4c).

Islands of zircon, domains of porosity, and porosity trails are less common in fragments reacted with the intermediate melt compared to the mafic melt (compare Figures 3–5). These microstructures share a similar abundance between the two mafic experiments of different durations (1 day vs. 3.5 days). Most fragments display homogeneous internal BSE and CL responses (Figures 3–5), but rare zircon fragments that were reacted with the intermediate melt show core to rim zonation in CL images (Figure 5c). In contrast, bands of bright CL response are coincident with the glass-filled channels and porosity trails identified in the BSE images of the zircon fragments and this response is more common in the mafic experiments (Figures 3c, 4b, f and 5h).

Raman spectra of zircon fragments reacted with intermediate melt are relatively uniform with a response of the $\upsilon_3(SiO_4)$ stretching band of 1008 cm^{-1} across the fragment (Figure 5d). In comparison, the response of zircon fragments reacted with mafic melt vary between 1008 and 1004 cm^{-1} (Figures 3d and 4d). The lowest response of the $\upsilon_3(SiO_4)$ stretching band coincides with the bright CL bands and glass-filled channels and porosity trails identified in the BSE images (Figures 3d and 4d).

3.2 | Glass Characterisation

Phenocrysts in the glass are observed in all experiments (Figures 3–5), but no mineral inclusions were identified in the glass-filled channels and pores within the zircon fragments. Phenocrysts in the intermediate melt comprised pyroxene, biotite, plagioclase, K-feldspar and apatite, whilst the melt in both mafic melt-zircon reaction experiments grew pyroxene and amphibole phenocrysts. Using a total alkali-silica (TAS) classification, the glass in the zircon-intermediate melt reaction experiment is andesitic, whereas the glass in the zircon-mafic melt reaction experiment is trachybasaltic (Data S1). These compositions are similar to the natural starting materials (Data S1). The analyses of the andesitic glass have relatively uniform SiO_2, Al_2O_3, K_2O and Na_2O, whereas other major elements are more variable (Data S1). Major element compositions of the glass within each of the mafic experiments are consistent except for FeO, MgO and inferred H_2O contents of the glass (Data S1). This is likely due to the different capsule material between the two experiments, with MO-21-47 experiencing Fe-loss to the Ag–Pd capsule.

Trace element analysis of the glasses showed large ion lithophile element (LILE) and light rare earth element (LREE)-enriched compositions similar to average crust (Data S4; Figure 6). Average La concentrations of glass in each experiment were 61 ppm (MO-20-21), 22,436 ppm (MO-21-43) and 10,007 ppm (MO-21-47) (Data S4). The Pb concentrations in the intermediate glass are higher (7–8 ppm) compared to the mafic glass (<0.1 ppm), whereas U concentrations are lower in the intermediate glass (2–3 ppm) relative to the mafic glass (3–15 ppm) (Data S4). As such, the Pb/U ratios are distinct for the two compositions of glass, with intermediate glass having a much higher average $^{207}Pb/^{235}U$ of 93.723 and $^{206}Pb/^{238}U$ of 0.804 relative to the mafic glass with an average $^{207}Pb/^{235}U$ of 1.667 and $^{206}Pb/^{238}U$ of 0.002 (Figure 6; Data S4).

3.3 | Trace Element and U–Pb Ages of Zircon Fragments

Trace element and U–Pb isotope analytical spot locations were guided by our microstructural characterisation of the zircon fragments (Section 3.1) to target low versus high proportions of glass filled channels and pores. The rare CL zonation observed in one fragment of the intermediate melt-zircon reaction experiment (Figure 5c) was too small to target. Mud Tank zircon has characteristically low trace element concentrations (Gain et al. 2019), such that we use elevated Ti and La as proxies for the proportions of glass inclusions within ablation volumes (Table S4). Mud Tank zircon has published median Ti and La concentrations of 4.25 ppm and 0.0118 ppm, respectively (Gain et al. 2019). Therefore, we classify zircon spots analyses with <5 ppm Ti and <0.2 ppm La concentrations ($n = 25$) as group 1 analyses (grey circle; Figure 6a). Zircon spot analyses with higher trace element concentrations (≥5 ppm Ti and ≥0.2 ppm La, $n = 51$) are hereafter referred to as group 2 analyses (diamonds, Figure 6a). The trace element concentrations of group 2 analyses form simple zircon-glass mixing arrays between the average of group 1 analyses (grey circle, Figure 6a) and the average glass chemistry of each experiment (red squares, Figure 6a). Group 2 analyses with the lowest La at a given Ti concentration are from the intermediate melt-zircon reaction experiment (MO-20-21, green outlined diamonds, Figure 6a). Those with moderate and high La at a given Ti concentration are from the mafic melt experiments MO-21-47 (light blue outlined diamonds, Figure 6a) and MO-21-43 (purple outlined diamonds, Figure 6a), respectively.

Group 1 analyses have uniform REE patterns similar to the median composition of Mud Tank zircon (black line, Figure 6b, c; Gain et al. 2019). Group 2 analyses show variable enrichment in LREE concentrations, with the highest variability observed for La concentrations and minor enrichment for Ce, Pr and Nd concentrations (light blue and purple lines, Figure 6b, c). La concentrations of group 2 analyses are more enriched in the mafic melt-zircon reaction experiments (Figure 6c). Both groups have overlapping concentrations of middle and heavy REE's and Th/U = 0.44–0.52 (Data S4).

Twenty-five signal selections were made from 25 spot analyses of the zircon fragments with low trace element concentrations (group 1 analyses), which spans across all three melt-zircon reaction experiments. The $^{206}Pb/^{238}U$ spot ages range between 744.2 ± 1.8 Ma and 721.7 ± 2.5 Ma, with a median spot age of 734.0 ± 2.6 Ma. The Concordia age of group 1 analyses is 736 ± 3 Ma ($n = 25$, MSWD = 1.7, $p(\chi^2) = 0.19$), whereas the $^{206}Pb/^{238}U$ weighted mean age is 734.8 ± 3.2 Ma ($n = 25$, MSWD = 0.55, $p(\chi^2) = 0.96$) (Figure 6d).

Thirteen signal selections from 13 spot analyses were chosen from zircon fragments within the intermediate melt-zircon experiments that have high trace element concentrations (group 2, i.e., ablation volumes with mixtures of zircon and small proportions of glass inclusions). Four U/Pb apparent ages are >5% discordant. The $^{206}Pb/^{238}U$ apparent ages of the concordant analyses range between 736.9 ± 1.9 and 654.5 ± 1.9 Ma, with a median apparent age 704.2 ± 1.9 Ma. The 13 analyses have a statistically invalid $^{206}Pb/^{238}U$ weighted mean age of 704.3 ± 3.7 Ma ($n = 13$, MSWD = 11, $p(\chi^2) = 0$) (Figure 6e).

Thirty-eight signal selections from 35 spot analyses were chosen from zircon fragments within the mafic melt-zircon reaction experiments that have high trace element concentrations (group 2, i.e., ablation volumes with mixtures of zircon and small proportions of glass inclusions). One U–Pb apparent age is >5% discordant. The $^{206}Pb/^{238}U$ apparent ages range between 751.0 ± 2.1 Ma and 647.4 ± 3.1 Ma, with a median apparent age 710.6 ± 1.8 Ma. The 38 analyses have a statistically invalid $^{206}Pb/^{238}U$ weighted mean of 708.0 ± 2.2 Ma ($n = 38$, MSWD = 11, $p(\chi^2) = 0$) (Figure 6f).

4 | Discussion

4.1 | Melt-Mediated Dissolution and Coupled Dissolution-Precipitation Replacement of Zircon

The rounded corners of the zircon fragments within the melt-zircon reaction experiments are interpreted to have formed from minor dissolution at fragment-melt interfaces (Figures 3e, 4b and 5f). Additionally, two types of melt-filled channels transect the reacted zircon fragments. The first type of melt-filled channels are oriented sub-parallel to the fragment edges, occur in sets and commonly transgress entire fragments ('glass-filled fracture', Figures 3–5). These are interpreted as melt infiltration along pre-existing fractures formed during crushing of the zircon fragments in preparation of the material for the experiment (Figure 2). The second type of melt-filled channels are discontinuous, may connect to fragment boundaries and/or terminate within fragments (black arrows, Figures 3–5). These show highly variable orientations relative to each other, display thickness variations along the channel and are spatially associated with abundant glass inclusions (black arrows, Figures 3–5). We interpret these dissolution channels formed by chemically driven instabilities emanating from the melt-zircon interface, similar to reaction infiltration instabilities recognised at sites of melt-rock and fluid-rock reactions (Chadam et al. 1986; Szymczak and Ladd 2014) and shown to develop in numerical experiments with high reaction rates and when advection dominates over diffusion (Koehn et al. 2021).

The glass-filled channels and pores are observed in most zircon fragments, indicating melt-zircon interaction was extensive. The smallest pores we can resolve with BSE imaging are <1 μm, but nanoscale pores may be distributed throughout the coupled dissolution-precipitation replacement textures. The domains that show higher proportions of melt within extensive channels (<7% area) are interpreted as areas of higher zircon dissolution relative to precipitation (Figure 4c). Glass-filled porosity is most extensive in zircon fragments adjacent to the glass-filled channels (Figures 3e, 4c and 5f, g). The glass-filled porosity may form trails with similar orientations to the glass-filled channels (Figure 4c and 5g). Some porosity trails transition to channels along strike (Figure 3b). These spatial patterns link the dissolution that forms the channels to a second process that creates the porosity within the zircon fragments.

The observation of distributed melt-filled porosity and porosity trails throughout the zircon fragments is indicative of melt-mediated coupled dissolution-precipitation replacement, where the zircon lattice is broken down and regrown (Putnis 2009). The porosity formed during coupled dissolution-precipitation replacement connects the reaction front to the reactant fluid source (Putnis, Tsukamoto, and Nishimura 2005) or, in our experiments, the bulk melt. With prolonged experiments, textural coarsening may heal porosity as the composition of the product mineral evolves toward equilibrium with the bulk fluid (Altree-Williams et al. 2015). Recently, coupled dissolution-precipitation melt-monazite reaction experiments showed crystal faces developed at melt-monazite interfaces (Varga et al. 2020). Similarly, some straight grain boundaries are recognised in our melt-zircon reaction experiments (red lines; Figures 3e and 4c) and are inferred as crystal facets. The straight grain boundaries could either result from precipitation of zircon against a melt film or from crystallographically controlled dissolution that minimises surface energy (Godinho, Piazolo, and Balic-Zunic 2014).

Raman mapping has been used to identify radiation damage of zircon, where zircon domains modified by high alpha doses exhibit changes to the response of Raman bands (Anderson et al. 2020). By analogy, defects within the zircon crystal lattice produced during coupled dissolution-precipitation replacement are inferred to cause the lower response of the $\upsilon_3(SiO_4)$ stretching band in our modified zircon domains (Figures 3d and 4d). Such defects include the porosity observed in BSE imaging (Figures 3–5), as well as nano-porosity, nano-inclusions, nano-fractures and other atomic-scale dislocations observed in studies using transmission electron microscopy and atom probe tomography (e.g., Seydoux-Guillaume et al. 2018). Our mafic

melt-zircon reaction experiments show a spatial relationship between domains of porous zircon, brighter CL response and lower response of the Raman $\upsilon_3(SiO_4)$ stretching band (Figures 3 and 4). Similarly, the intermediate melt-zircon reaction experiment has the same correlation between domains of zircon porosity and brighter CL response (Figure 5g, h) and also shows one fragment with a darker CL response rim that correlates with lower response of the Raman $\upsilon_3(SiO_4)$ stretching band (Figure 5c, d). Therefore, Raman mapping of natural complicated zircons may help identify domains that experienced coupled dissolution-precipitation replacement.

The mafic melt-zircon reaction experiments show higher proportions of glass-filled channels and pores, and greater variation in the Raman maps compared to the intermediate melt-zircon reaction experiment (Figures 3–5), suggesting a dominance of dissolution over precipitation during coupled dissolution-precipitation replacement in mafic melts. This observation is supported by experiments that determine higher zircon solubility in mafic melts (Borisov and Aranovich 2019) and has implications for the survival and degree of modification of xenocrysts in magmas of different compositions. We only observed the development of core-rim textures in the intermediate melt-zircon reaction experiments (Figure 5c), also showing how the different melt compositions drive different styles of coupled dissolution-precipitation replacement. We do not observe differences in the microstructure of the two mafic melt-zircon reaction experiments which ran for 1 day and 3.5 days, demonstrating that the process is geologically very fast and that the duration of the experiments had little consequence for the microstructural patterns developed during zircon coupled dissolution-precipitation replacement.

Natural zircon grains show the same channels and pores (Figure 1) as developed in our reaction experiments (Figures 3–5). However, minerals such as plagioclase, amphibole, and quartz, fill the channels and pores in the natural zircon grains (Figure 1). This suggests that these minerals are epigenetic inclusions that crystallised during melt-zircon interaction and that care is needed when interpreting inclusion assemblages in zircon. The natural zircon xenocrysts in granite show modified and truncated CL patterns with minor dissolution altering primary grain shapes (Figure 1a). Bright CL response mantles are discontinuous at core-rim boundaries in zircon xenocrysts from granite (Figure 1a). In contrast, bright CL response domains form rims or cross-cutting bands in zircon xenocrysts from the layered mafic-ultramafic intrusion (Figure 1b). The bright CL band is coincident with a plagioclase-filled dissolution channel (Figure 1b) and is similar to the microstructures formed within our mafic melt-zircon reaction experiments (Figures 3, 4). Zircon modified by mafic melts migrating through high strain zones in New Zealand are also dissected by many plagioclase and amphibole filled dissolution channels (Figure 1c). Orientation patterns of these dissolution channels (Figure 1c) are comparable to the glass-filled channels and trails within all our melt-zircon reaction experiments (Figures 3 and 4).

The networks of bright CL bands in reacted zircon from our experiments (Figures 3c, 4b and 5h) are similar to those observed in zircon from meteorite impact sites (Cavosie, Erickson, and Timms 2015; Cavosie et al. 2010; Montalvo et al. 2019) and migmatitic granite (Rimša et al. 2007). These bright CL rims, bands and networks are formed by secondary zircon that precipitated by melt ingress into shock fractures (Cavosie, Erickson, and Timms 2015; Montalvo et al. 2019) or hydrothermal fluid ingress into hydraulic fractures (Rimša et al. 2007). The new bright CL zircon from the migmatitic granite has low Th content and is LREE enriched relative to the precursor zircon (Rimša et al. 2007), possibly indicating that the zircon chemistry changed. Our experiments show that these chemical patterns could be due to analysis of micro-inclusions (Figure 6). The indistinguishable geochemistry between primary and secondary zircon within shocked zircon (Cavosie, Erickson, and Timms 2015) suggests the CL bright response is caused by defects within the zircon (i.e., fractures and pores inclusions) introduced during coupled dissolution-precipitation replacement, rather than a chemical change. Zircon from meteorite impact sites also commonly shows external granular textures (Cavosie, Erickson, and Timms 2015; Cavosie et al. 2010; Montalvo et al. 2019), which resemble the grain boundary morphology of the reacted zircons in our experiments (red lines, Figures 3e and 4c). We propose melt-zircon interaction might play a role in forming the external granular textures of shocked zircons.

All the key microstructures observed in the natural zircon case studies discussed above formed during our melt-zircon reaction experiments in remarkably short time periods. Therefore, we provide the first experimental evidence to support the published interpretations of melt-mediated modification of the natural zircons (Cavosie, Erickson, and Timms 2015; Cavosie et al. 2010; Halpin et al. 2020; Montalvo et al. 2019; Spier, Filho, and Daczko 2022; Spier, Daczko, and Zhou 2024). Whilst many studies interpret hydrothermal fluids mediated coupled dissolution-precipitation replacement of zircon, the tectonic settings and histories of the host rocks involves earlier high temperature magmatic or high-grade metamorphic events and opens melt-mediated coupled dissolution-precipitation replacement as a viable mechanism to explain these textures (e.g., Kelly et al. 2017; Vonlanthen et al. 2012; Schwartz et al. 2010). For example, highly porous zircon at mid-ocean ridges (e.g., Cavosie, Kita, and Valley 2009; Schwartz et al. 2010) and in high-grade metamorphic rocks (Kelly et al. 2017; Vonlanthen et al. 2012) may have been modified by melt interaction during the higher temperature history of these rocks. We suggest that the timing of coupled dissolution-precipitation replacement requires careful consideration to evaluate if it formed during melt-present conditions or subsequent alteration from hydrothermal fluids.

4.2 | Low Mobility of Trace Elements and Radiogenic Pb During Zircon Coupled Dissolution-Precipitation Replacement

The trace element concentrations of zircon spot analyses (Section 3.3) demonstrate that few zircon domains lack glass inclusions and retain the original Mud Tank zircon chemistry and age (group 1 analyses; Figure 6), whilst many ablation volumes included some glass as indicated by enriched Ti and La concentrations (group 2 analyses; Figure 6). We interpret group

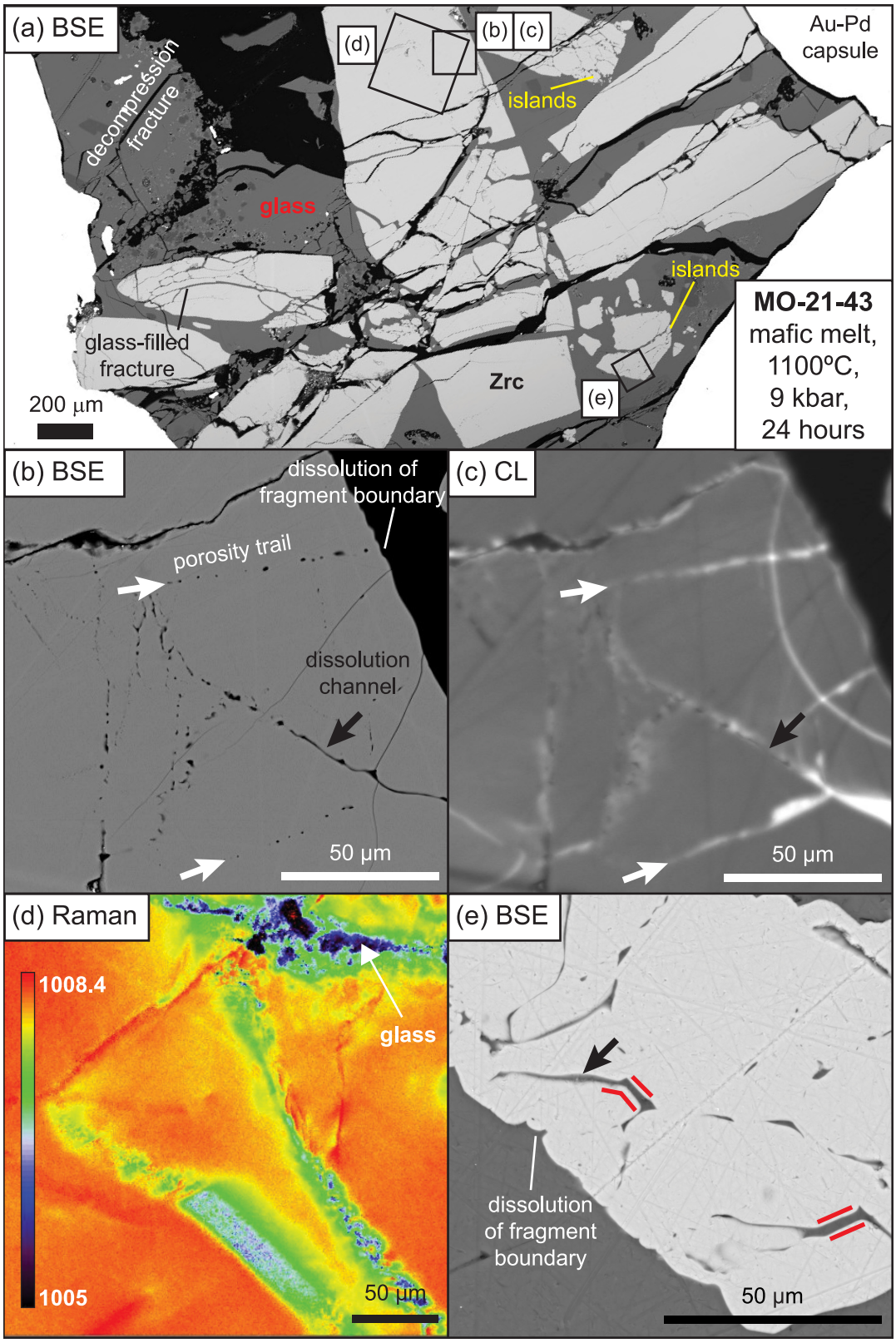

FIGURE 3 | Microstructural characterisation of mafic melt-zircon reaction experiment MO-21-43. (a) Overview image displays the zircon fragments (light grey) in quenched glass (dark grey) within the experimental capsule (white). (b, e) Backscattered electron images display porosity trails (white arrows), dissolution channels (black arrows), dissolution of fragment boundaries and short segments of faceted edges (red lines), which are indicative of areas replaced by zircon coupled dissolution-precipitation replacement. Porosity trails and dissolution channels are associated with brighter CL responses (c) and lower responses of the $\upsilon_3(SiO_4)$ stretching band (cm^{-1}) in Raman mapping (d). Note that the experimental block was polished several times in between analytical techniques to ensure optimum outcomes. Therefore, subtle differences in microstructure are observed between panels.

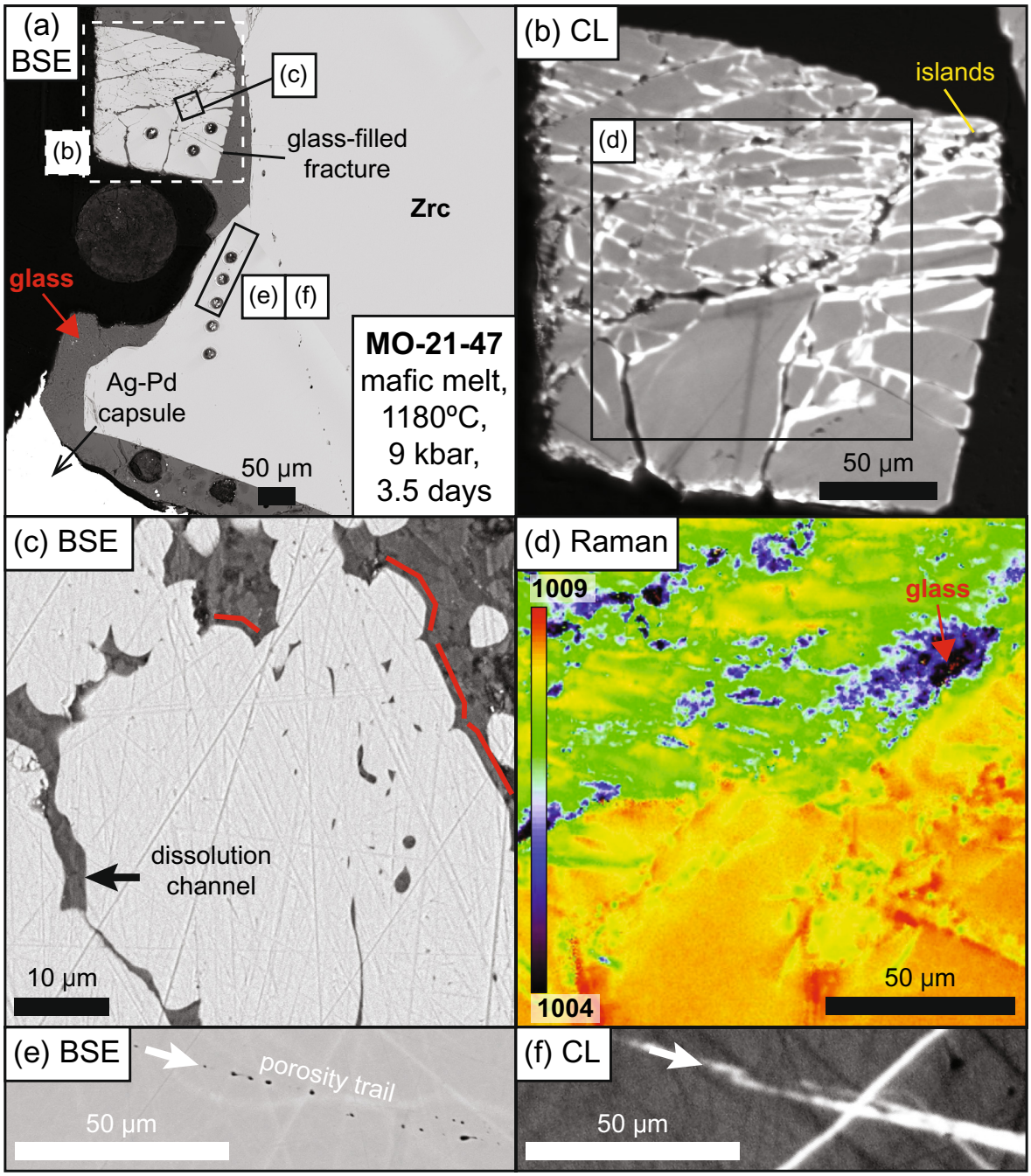

FIGURE 4 | Microstructural characterisation of mafic melt-zircon reaction experiment MO-21-47. Annotations follow Figure 3. Note that the experimental block was polished several times in between analytical techniques to ensure optimum outcomes. Therefore, subtle differences in microstructure are observed between panels.

1 analyses are unmodified Mud Tank zircon and group 2 analyses are from zircon domains modified by coupled dissolution-precipitation replacement. Nearly all the zircon trace element concentrations lie upon a mixing line between the average unmodified Mud Tank zircon and the glass composition of each experiment (Figure 6a). This implies that replaced zircon has low trace element concentrations like the unmodified Mud Tank zircon (Gain et al. 2019). Perhaps a precursor zircon that was richer in non-essential cations (REE, Y, Th and U) might experience greater chemical modification within the experimental timeframe and this highlights new experiments that modify a trace element rich zircon are needed.

The unmodified zircon spot analyses (group 1) yield uniform concordant U–Pb age data ($^{206}Pb/^{238}U$ weighted mean age = 734.8 ± 3.2 Ma) within error of the known age of Mud Tank zircon (730 ± 10 Ma; Gain et al. 2019) (Figure 6d). This confirms that these zircon domains were not modified in the experiments. The zircon spot analyses from domains replaced by coupled dissolution-precipitation (group 2) mostly overlap the concordant unmodified zircon data, but some analyses smear to younger ages with or without increased discordance (Figure 6e, f). Simple isotope mixing models between unmodified zircon and the two glass compositions predict that the ablation of increasing proportions of glass inclusions will shift data to higher

$^{206}Pb/^{238}U$ and $^{207}Pb/^{235}U$ for the intermediate melt-zircon reaction experiment, compared with lower ratios for the mafic experiments (red arrows, Figure 6e, f). The zircon analyses from the intermediate melt-zircon reaction experiment do not lie along the isotope mixing model (red arrow, Figure 6e), suggesting another process contributed to the dispersion of age data on the Terra-Wasserburg diagrams, such as Pb-loss from the zircon to the bulk melt and/or variable redistribution of Pb within a fragment during coupled dissolution-precipitation replacement.

This smearing dispersion in the data is best explained by variable degrees of ablating glass inclusions (red arrow, Figure 6e) and Pb loss (dashed black arrow, Figure 6e), driving higher $^{207}Pb/^{235}U$ and lower $^{206}Pb/^{238}U$ values, respectively. For example, the trace element chemistry of the spot analysis with the youngest $^{206}Pb/^{238}U$ age (green bold outline, Figure 6e) indicates ~3% of its ablation volume was intermediate glass inclusions (Table S4). Therefore, an additional ~12% Pb-loss from the replaced zircon domain is required to explain the data plotted on the Terra-Wasserburg diagram (Figure 6e). In comparison, zircon ages from the mafic melt-zircon experiments are dispersed along the simple isotope mixing model (red arrow, Figure 6e) which lies sub-parallel to the Pb loss trend (dashed black arrow, Figure 6f) and the Concordia line. In these experiments, combinations of Pb-loss and ablation of glass inclusions is also required to explain the dispersion of the data (Figure 6f). Of interest, the two youngest zircon spot analyses include one ablation volume containing ~25% glass inclusions and another with only 0.6% (bold purple outlines, Figure 6f). These two analyses can only be explained by variable degrees of Pb-loss from the replaced zircon domains, ranging up to 10% (dashed black arrow, Figure 6f). Dating of both oscillatory zoned and bright CL response domains in migmatitic granite, southwest Sweden, shows dispersion of ages over hundreds of millions of years (Rimša et al. 2007) and is an example of how challenging it is to interpret these complex age arrays in natural rocks.

Presumably, continued coupled dissolution-precipitation replacement during longer experiments and in nature would facilitate more Pb loss. In nature, slower cooling from melt-present conditions would promote crystallisation and formation of mineral inclusions in contrast to the glass inclusions within the experiments. However, ablation of any inclusions will mask the true zircon trace element geochemistry and possibly disturb U–Pb age patterns (Zhong et al. 2018). Our experiments demonstrate care is needed when interrogating the geochemistry of zircon modified by coupled dissolution-precipitation replacement.

4.3 | Multiple Cycles of Coupled Dissolution-Precipitation

The development of intracrystalline porosity in minerals undergoing coupled dissolution-precipitation replacement is driven by a volume deficit arising from the differing solubilities of reactant and product minerals within the local fluid or melt. This process may be further influenced by variations in molar volumes between the reactants and products (Putnis 2009). In our melt-zircon reaction experiments, despite minimal differences in molar volumes between Mud Tank zircon and the replaced zircon, the higher solubility of Mud Tank zircon within the local

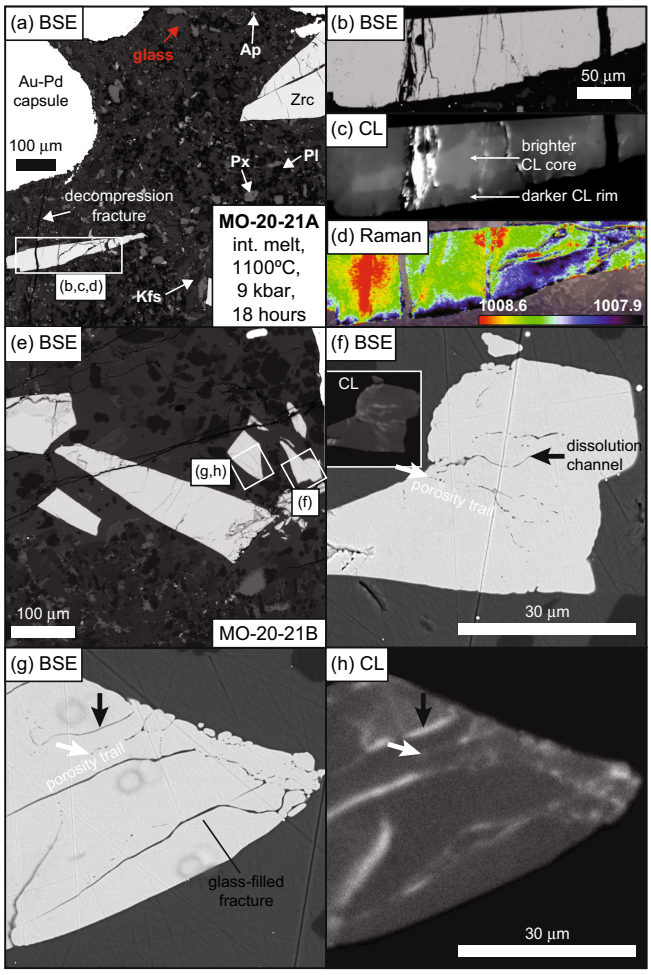

FIGURE 5 | Microstructural characterisation of intermediate melt-zircon reaction experiment MO-20-21. Annotations follow Figure 3. Note additionally that microstructures indicative of zircon coupled dissolution-precipitation replacement are less common in this experiment relative to the mafic melt-zircon reaction experiments. One fragment developed a core-rim texture visible in CL imagery (c) that was not observed in the mafic-melt experiments. Phenocryst labels follow: Ap = apatite, Pl = plagioclase, Px = pyroxene and Kfs = K-feldspar. Note that the experimental block was polished several times in between analytical techniques to ensure optimum outcomes. Therefore, subtle differences in microstructure are observed between panels.

melt is identified as the primary cause of intracrystalline porosity in the replaced zircon.

Numerous studies assert that mass transport through porous and permeable product minerals links the bulk fluid with the reaction front. The progression of the replacement reaction into the reactant mineral relies on the sustained connectivity of porosity (Putnis 2009). Notably, experiments replacing KBr with KCl resulted in the development of coarse interconnected pores, visible through scanning electron microscopy (Putnis 2009) and X-ray computed micro-tomography (Beaudoin et al. 2018), emphasising the high permeability within replaced domains. This evidence suggests a one-step process of coupled dissolution-precipitation replacement, with textural equilibration subsequently reducing reaction intensity through coarsening and decreasing porosity connectivity

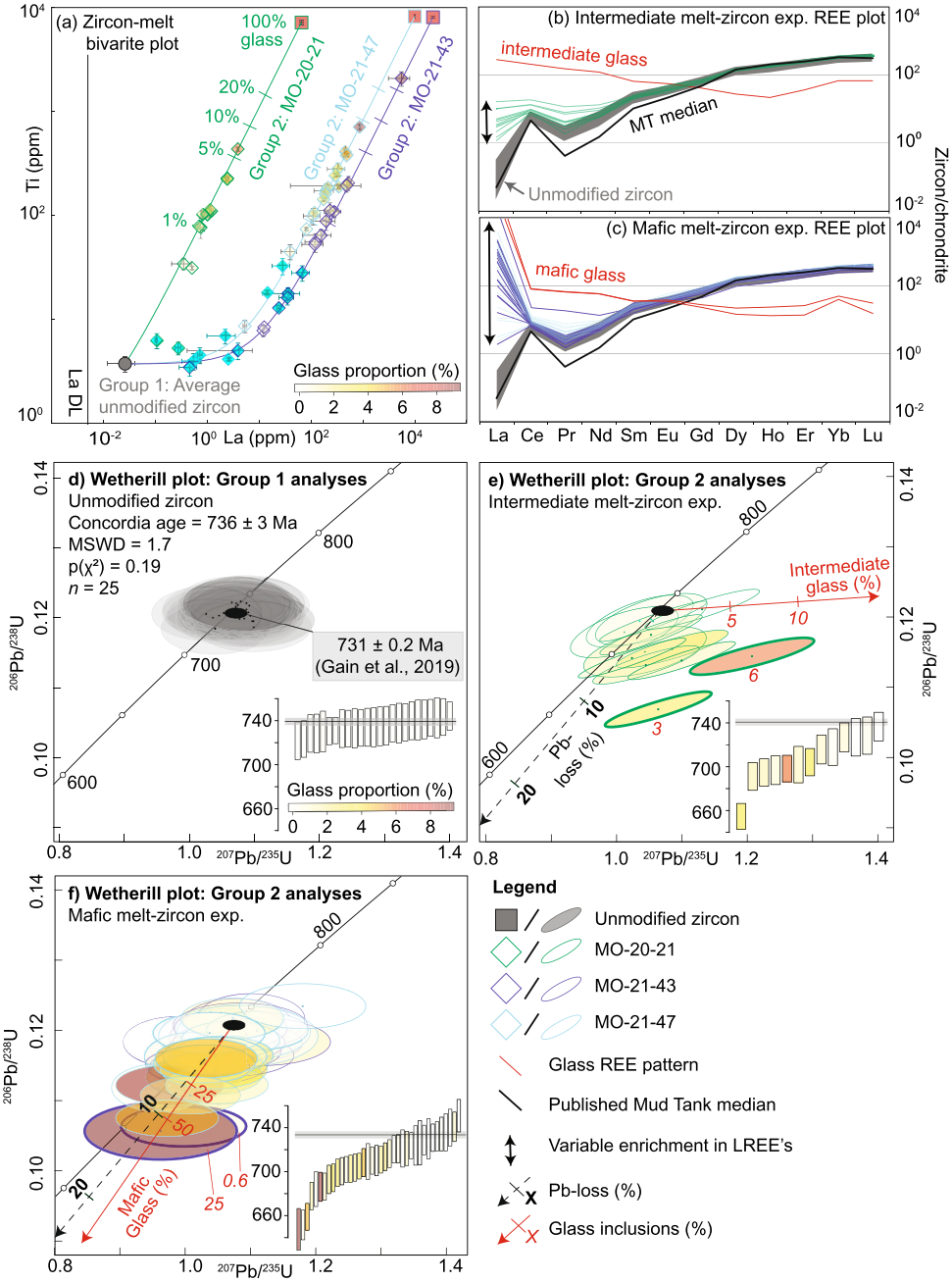

FIGURE 6 | LA-ICPMS geochemical and isotopic characterisation of zircon fragments within the melt-zircon reaction experiments. Grey shapes indicate spot analyses of unmodified zircon (group 1 analyses), whereas green, purple and light blue shapes identify spot analyses of modified zircon domains from experiments MO-20-21, MO-21-43 and MO-21-47, respectively (group 2 analyses). (a) Log–log plot of Ti versus La concentrations of zircon spot analyses. The coloured diamonds are zircon spot analyses with elevated trace element concentrations (group 2 analyses). These analyses primarily lie on mixing trends (coloured lines) between average unmodified zircon (grey circle; group 1 analyses) and the average composition of glass in each experiment (red squares). Error bars represent 95% confidence, DL = detection limit and the Ti detection limit is <1. Chondrite-normalised rare earth element plots of the (b) intermediate melt-reaction experiment and (c) mafic melt-reaction experiments show variable enrichment in light rare earth elements (double headed black arrows). We interpret this enrichment is due to variable proportions of glass inclusions within the zircon ablation volume and this enrichment trends toward the glass composition of each experiment (red lines). The grey shaded area denotes the rare earth element patterns of unmodified zircon, whereas the solid black line is median rare earth element concentrations of Mud Tank zircon published in Gain et al. (2019). Wetherill and $^{206}Pb/^{238}U$ weighted mean age plots of unmodified Mud Tank zircon (d), modified zircon from the intermediate melt-zircon experiment (e), and modified zircon from the mafic melt-zircon experiments (f), produced using IsoplotR (Vermeesch 2018). The black line and transparent grey bar on the weighted mean plot in each panel represents the weighted mean age and 2σ of the unmodified zircon analyses (Group 1). Zircon spot analyses (circles delineate 95% confidence) from the intermediate melt-zircon reaction experiment smear to younger ages along a discordant trend (e), whereas spot analyses from the mafic melt-zircon reaction experiments smear to younger ages along a near-concordant trend (f). Both trends can only be explained if the ablation volume of zircon contains a mixture of glass inclusions (red lines) and zircon that has experienced Pb-loss (dashed black line) facilitated by coupled dissolution-precipitation replacement during melt-zircon reaction. Bolded outlines indicate individual spot analyses discussed within the text.

(Beaudoin et al. 2018; Putnis, Tsukamoto, and Nishimura 2005; Putnis and Mezger 2004).

In certain experiments, nano-porosity is apparent only under transmission electron microscopy (e.g., Harlov, Wirth, and Förster 2005). However, the true connectedness of this nano-porosity remains a matter of interpretation, raising questions about the perfect permeability of the product mineral (Norberg et al. 2011). This uncertainty leads to the proposal of multi-stage coupled dissolution-precipitation replacement scenarios, where the composition of the precipitated mineral varies within replaced domains due to restrictions on diffusion and equilibration imposed by the nano-porous structure (Borg et al. 2014; Norberg et al. 2011).

The intricate nature of these processes suggests that, over time, chemical equilibration between the product mineral and bulk fluid may occur through repeated cycles of coupled dissolution-precipitation (Borg et al. 2014; Norberg et al. 2011). In scenarios where the composition of the precipitated mineral is variable due to kinetic and local conditions at the reaction front, or where the porous product mineral is not perfectly permeable, achieving a homogeneous composition in equilibrium with the bulk fluid necessitates multiple cycles of coupled dissolution-precipitation replacement. In natural open systems where fluids or melts migrate through rocks, variations in the 'bulk' fluid or melt composition during geological events are probable, emphasising the likelihood of repeated cycles of coupled dissolution-precipitation replacement as reactions progress (Altree-Williams et al. 2015). As such, we predict that repeated cycles of coupled dissolution-precipitation replacement of zircon will enhance Pb-loss leading to the eventual resetting of the age of the replaced zircon domain. Any replaced zircon that does not reach this end point will have a spurious age.

Despite observations and implications of connected micro- and nano-porosity in experiments, it is noted that such microstructures are less likely to persist in natural samples over extended geological time periods (Harlov, Wirth, and Förster 2005). As such, a perfectly interconnected porosity is unlikely to be preserved in natural minerals. Nonetheless, the preservation of some porous microstructure is a hallmark of former coupled dissolution-precipitation replacement reactions (Putnis 2009).

4.4 | Duration of Geological Events, Spurious Ages, and Criteria for Recognition of Former Coupled Dissolution-Precipitation in Zircon

Coupled dissolution-precipitation replacement in the melt-zircon reaction experiments involves the breakdown of the original Mud Tank zircon crystal lattice through dissolution and replacement by a newly crystallised lattice, which is in chemical equilibrium with the boundary fluid (Putnis 2009). As such, all radiogenic Pb which is incompatible in the zircon lattice is expected to partition into the interfacial melt as the original zircon is dissolved (Figure 7a). However, the degree of replacement and the nanoscale distribution of melt inclusions is not resolved by BSE imaging, and this results in ablation volumes comprising variable proportions of possibly unmodified Mud Tank zircon, replaced zircon, and melt inclusions rich in Pb expelled from the

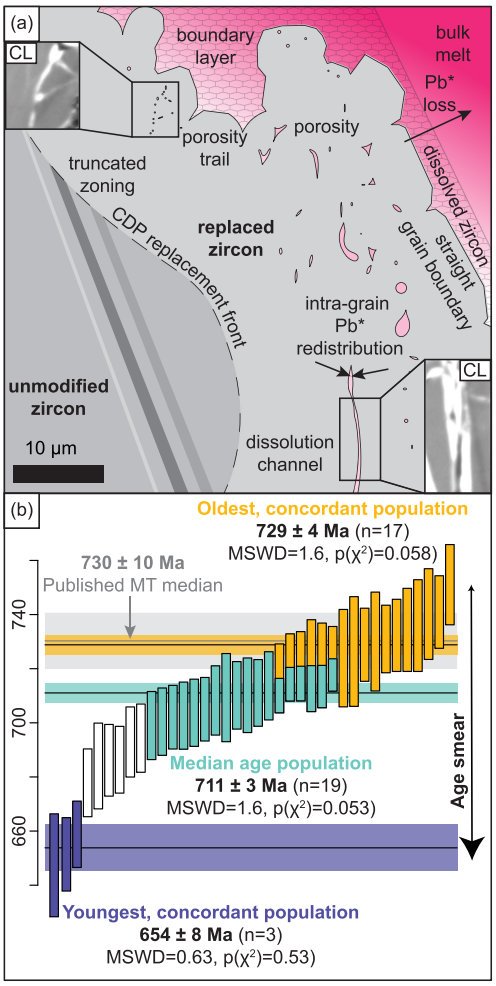

FIGURE 7 | (a) Summary cartoon of melt-mediated based, coupled dissolution-precipitation replacement of zircon fragments in the zircon-melt reaction experiments. A dashed line represents the replacement front between unmodified Mud Tank zircon and zircon replaced by coupled dissolution-precipitation. This replacement front causes truncated and convolute zoning between zircon domains. Rounded corners and embayments in the zircon fragment edge, coupled with short, faceted zircon edges occur during dynamic dissolution and precipitation of the zircon fragment edge. The domains of replaced zircon contain dissolution channels, porosity trails and distributed porosity that are filled with quenched glass. An interfacial boundary melt (patterned area) develops which is enriched in dissolved zircon compared to the bulk melt (darker pink area). Communication between the melt inclusions within the dynamic porosity and channels within zircon and the boundary layer melt allows the radiogenic Pb (Pb*) from the dissolved zircon to escape into the melt-filled channels and pores and diffuse to the bulk melt via the boundary layer melt. (b) $^{206}Pb/^{238}U$ weighted mean age plot of the mafic-melt zircon reaction experiments. With this data, three common statistical approaches to the near-concordant age smear are applied: (orange) the oldest, concordant population is interpreted as the protolith age, (teal) a statistically valid population around the median age is interpreted as the crystallisation age and (purple) the youngest, concordant population is interpreted as the age of a resetting or metamorphic event. Only the first approach produces a 'geologically meaningful age' within the scope of the zircon melt-reaction experiments, that is, it correctly determines the protolith age of the zircon. The other statistical approaches produce two meaningless younger ages that in a natural rock would confuse the geological evolution.

replaced Mud Tank zircon. The U–Pb age results of the ablation volumes demonstrate that coupled dissolution-precipitation replacement of zircon does not completely reset the zircon age (Figure 6). Instead, the ablation of our replaced zircon volumes produces a dispersed age dataset with concordant ages that are smeared over 100 million years from the known Mud Tank age (Figures 6 and 7b). This spread of near concordant spot analyses was produced from experiments that ran from hours to days, questioning how geologically meaningful these age patterns are in natural rocks. Whilst many studies have used these age patterns in single samples as evidence for long-lived geological events (e.g., He et al. 2018; Korhonen et al. 2013), we caution that other scenarios are possible.

All the spot ages of replaced zircon in our melt-zircon reaction experiments are spurious since the replaced zircon crystallised at 0 Ma. This poses problems for igneous rocks with solely xenocrystic zircons (particularly mafic rocks) where coupled dissolution-precipitation replacement of the xenocrysts by the host magma may not necessarily reset the age of zircons to the plutonic age (Halpin et al. 2020). In melt-bearing, high-temperature metamorphic rocks, melt-zircon interaction may similarly form complicated and spurious smeared age patterns, which may incorrectly record the age and duration of metamorphism (Halpin et al. 2012). This problem is particularly challenging in scenarios where ages are smeared over shorter time periods, for example, 10–20 million years (Milan et al. 2016). Statistical approaches to these smeared age datasets are biased to concordant and median ages, such that the calculated age is unlikely to be geologically meaningful. Furthermore, we predict that the porous character of zircon replaced by coupled dissolution-precipitation replacement may make this zircon more susceptible to younger Pb-loss events, such as during lower temperature metamorphic or hydrothermal alteration (e.g., Kelly et al. 2017; Vonlanthen et al. 2012).

Given these geochronological challenges, we summarise key criteria that can be used to identify former zircon coupled dissolution-precipitation replacement as evidenced by the melt-zircon reaction experiments. The most reliable microstructural criteria are (1) microporosity, patchily distributed or in trails, (2) inclusions, (3) rounded crystal terminations and other evidence of dissolution textures at grain boundaries (e.g., embayments), and (4) blurred, convoluted, and truncated CL patterns (Figure 7a). Other supporting criteria we promote are (5) lower response of Raman stretching bands and (6) anomalous zircon trace element and isotope chemistry, such as decoupling between age and trace element chemistry patterns. Additional information that may be able to help distinguish between replaced zircon versus a new zircon overgrowth may be obtained using EBSD analysis, since the crystal lattice of replaced zircon should display apparent bending and the development of sub grain domains (Spruzeniece, Piazolo, and Maynard-Casely 2017).

Once zircon coupled dissolution-precipitation replacement is recognised as such, the geochronological data can be interrogated in different ways. One traditional approach to dispersed age data sets is to exclude some younger grains due to Pb-loss and some older grains due to near crystallisation age inheritance to produce a statistically valid single population (e.g., Craven, Daczko, and Halpin 2012). For example, if the mafic melt-zircon reaction experiment was a natural age dataset, this approach would produce an age of 711 ± 3 Ma (teal, Figure 7b). This age is 20 million years younger than Mud Tank zircon (Gain et al. 2019) and this age is >711 million years older than the coupled dissolution-precipitation replacement event, such that neither geological event is correctly dated. Another traditional approach to dispersed age data sets is to focus on the oldest population of spot analyses to determine a protolith age (Halpin et al. 2012) and the youngest population to date the resetting event (e.g., Yin et al. 2010). Again, if the mafic experiments were a natural dataset, we could interpret a protolith age of 729 ± 4 Ma (orange, Figure 7b) and a metamorphic age of 654 ± 8 Ma (purple, Figure 7b). Alternatively, if the oldest spot analysis was used as the protolith age, an interpretation of 751 ± 2 Ma might be presented (Halpin et al. 2012). The only correct age among these traditional approaches is the protolith age based on the oldest population and none of these approaches identify the recent (0 Ma) metamorphic age. Our experiments establish the importance of understanding processes such as coupled dissolution-precipitation replacement when interpreting complex geochronological data. Such data should be treated carefully and in the context of regional studies that date other (less complicated) samples, and which use minerals not modified by coupled dissolution-precipitation replacement.

5 | Conclusion

The characterised melt-zircon reaction experiments provide the first experimental evidence of melt-mediated coupled dissolution-precipitation replacement of zircon. The zircon fragments within the experiments developed glass-filled channels and pores indicative of coupled dissolution-precipitation replacement and the zircon spot data reveals a dispersed age dataset, reflecting varying degrees of Pb-loss during the replacement process. Recognising coupled dissolution-precipitation replacement in zircon involves considering multiple criteria, such as the presence of microporosity, inclusions, rounded crystal terminations, and modified cathodoluminescence (CL) patterns. Raman mapping emerges as a valuable tool for identifying zircon domains affected by coupled dissolution-precipitation replacement. Our study postulates that recurrent cycles of coupled dissolution-precipitation might intensify Pb-loss, ultimately resulting in the resetting of the age of replaced zircon domains. The findings from our experiments provide essential insights into the complexities of coupled dissolution-precipitation replacement in zircon, emphasising the necessity for a cautious and nuanced interpretation of geochronological data.

Acknowledgements

We acknowledge Karsten Goemann at the Central Science Laboratory (CSL), University of Tasmania and Sean Murray of Macquarie University GeoAnalytical (MQGA), for facilitating laboratory analyses used in this study. We further thank Elena Belousova for providing the Mud Tank starting material and for constructive discussions on the experimental design and project plan. This study was financially supported internally through the School of Natural Sciences, Macquarie University, and by the Geological Society of Australia, through the GSA endowment fund. I.S.E. acknowledges funding from

Stephen Foley's ARC Laureate Fellowship FL180100134. J.A.H was supported by the ARC Special Research Initiative, Australian Centre for Excellence in Antarctic Science (Project Number SR200100008). We thank Aaron Cavosie and Bernardo Cesare for their careful and constructive reviews and Bernardo Cesare for editorial handling.

Data Availability Statement

The data that supports the findings of this study are available in the supplementary material of this article

References

Altree-Williams, A., A. Pring, Y. Ngothai, and J. Brugger. 2015. "Textural and Compositional Complexities Resulting From Coupled Dissolution-Reprecipitation Reactions in Geomaterials." *Earth-Science Reviews*. 150: 628–651. https://doi.org/10.1016/j.earscirev.2015.08.013.

Anderson, A. J., J. M. Hanchar, K. V. Hodges, and M. C. van Soest. 2020. "Mapping Radiation Damage Zoning in Zircon Using Raman Spectroscopy: Implications for Zircon Chronology." *Chemical Geology* 538: 119494. https://doi.org/10.1016/J.CHEMGEO.2020.119494.

Asimus, J. L., N. R. Daczko, and I. S. Ezad. 2023. "Melt-Present Deformation at the Entia Dome, Central Australia: A Metamorphic Core Complex Formed During Lower Crustal Tectonic Extrusion." *Lithos* 448–449: 107170. https://doi.org/10.1016/J.LITHOS.2023.107170.

Baker, J., D. Peate, T. Waight, and C. Meyzen. 2004. "Pb Isotopic Analysis of Standards and Samples Using a 207Pb–204Pb Double Spike and Thallium to Correct for Mass Bias With a Double-Focusing MC-ICP-MS." *Chemical Geology* 211: 275–303. https://doi.org/10.1016/J.CHEMGEO.2004.06.030.

Beaudoin, N., A. Hamilton, D. Koehn, Z. K. Shipton, and U. Kelka. 2018. "Reaction-Induced Porosity Fingering: Replacement Dynamic and Porosity Evolution in the KBr-KCl System." *Geochimica et Cosmochimica Acta* 232: 163–180. https://doi.org/10.1016/J.GCA.2018.04.026.

Belousova, E. A., W. L. Griffin, S. Y. O'Reilly, and N. I. Fisher. 2002. "Igneous Zircon: Trace Element Composition as an Indicator of Source Rock Type." *Contributions to Mineralogy and Petrology* 143: 602–622. https://doi.org/10.1007/s00410-002-0364-7.

Black, L. P., S. L. Kamo, C. M. Allen, et al. 2004. "Improved $^{206}Pb/^{238}U$ Microprobe Geochronology by the Monitoring of a Trace-Element-Related Matrix Effect; SHRIMP, ID–TIMS, ELA–ICP–MS and Oxygen Isotope Documentation for a Series of Zircon Standards." *Chemical Geology* 205: 115–140. https://doi.org/10.1016/J.CHEMGEO.2004.01.003.

Borg, S., W. Liu, M. Pearce, J. Cleverley, and C. MacRae. 2014. "Complex Mineral Zoning Patterns Caused by Ultra-Local Equilibrium at Reaction Interfaces." *Geology* 42: 415–418. https://doi.org/10.1130/G35287.1.

Borisov, A., and L. Aranovich. 2019. "Zircon Solubility in Silicate Melts: New Experiments and Probability of Zircon Crystallization in Deeply Evolved Basic Melts." *Chemical Geology* 510: 103–112. https://doi.org/10.1016/j.chemgeo.2019.02.019.

Cavosie, A. J., T. M. Erickson, and N. E. Timms. 2015. "Nanoscale Records of Ancient Shock Deformation: Reidite ($ZrSiO_4$) in Sandstone at the Ordovician Rock Elm Impact Crater." *Geology* 43, no. 4: 315–318. https://doi.org/10.1130/G36489.1.

Cavosie, A. J., N. T. Kita, and J. W. Valley. 2009. "Primitive Oxygen-Isotope Ratio Recorded in Magmatic Zircon From the Mid-Atlantic Ridge." *American Mineralogist* 94, no. 7: 926–934. https://doi.org/10.2138/am.2009.2982.

Cavosie, A. J., R. R. Quintero, H. A. Radovan, and D. E. Moser. 2010. "A Record of Ancient Cataclysm in Modern Sand: Shock Microstructures in Detrital Minerals From the Vaal River, Vredefort Dome, South Africa." *GSA Bulletin* 122, no. 11–12: 1968–1980. https://doi.org/10.1130/B30187.1.

Chadam, J., D. Hoff, E. Merino, P. Ortoleva, and A. Sen. 1986. "Reactive Infiltration Instabilities." *IMA Journal of Applied Mathematics* 36: 207–221. https://doi.org/10.1093/IMAMAT/36.3.207.

Charlier, B. L. A., C. J. N. Wilson, J. B. Lowenstern, S. Blake, P. W. van Calsteren, and J. P. Davidson. 2005. "Magma Generation at a Large, Hyperactive Silicic Volcano (Taupo, New Zealand) Revealed by U-Th and U-Pb Systematics in Zircons." *Journal of Petrology* 46: 3–32. https://doi.org/10.1093/petrology/egh060.

Cherniak, D. J., and E. B. Watson. 2003. "Diffusion in Zircon." *Reviews in Mineralogy and Geochemistry* 53: 113–143. https://doi.org/10.2113/0530113.

Cherniak, D. J., and E. B. Watson. 2001. "Pb diffusion in Zircon." *Chemical Geology* 172: 5–24. https://doi.org/10.1016/S0009-2541(00)00233-3.

Craven, S. J., N. R. Daczko, and J. A. Halpin. 2012. "Thermal Gradient and Timing of High-T–Low-P Metamorphism in the Wongwibinda Metamorphic Complex, Southern New England Orogen, Australia." *Journal of Metamorphic Geology* 30: 3–20. https://doi.org/10.1111/J.1525-1314.2011.00949.X.

Daczko, N. R., and J. A. Halpin. 2009. "Evidence for Melt Migration Enhancing Recrystallization of Metastable Assemblages in Mafic Lower Crust, Fiordland, New Zealand." *Journal of Metamorphic Geology* 27: 167–185. https://doi.org/10.1111/j.1525-1314.2009.00811.x.

Daczko, N. R., S. Piazolo, U. Meek, C. A. Stuart, and V. Elliott. 2016. "Hornblendite Delineates Zones of Mass Transfer Through the Lower Crust." *Scientific Reports* 6: 1–6. https://doi.org/10.1038/srep31369.

Elliot, V. 2016. *Zircon Growth and Modification During Deep Melt Flux Through a Magmatic arc*. M. Research thesis. Sydney Australia: Macquarie University.

Ezad, I. S., S. S. Shcheka, S. Buhre, et al. 2023. "Rapid Quench Piston Cylinder Apparatus: An Improved Design for the Recovery of Volatile-Rich Geological Glasses From Experiments at 0.5-2.5 GPa." *Review of Scientific Instruments* 94: 1–12. https://doi.org/10.1063/5.0129417.

Fougerouse, D., T. Geisler, S. M. Reddy, et al. 2024. "Melt-Mediated Re-Equilibration of Zircon Produced During Meltdown of the Chernobyl Reactor." *American Mineralogist* 109: 8–14. https://doi.org/10.2138/am-2022-8824.

Gain, S. E. M., Y. Gréau, H. Henry, et al. 2019. "Mud Tank Zircon: Long-Term Evaluation of a Reference Material for U-Pb Dating, Hf-Isotope Analysis and Trace Element Analysis." *Geostandards and Geoanalytical Research* 43: 339–354. https://doi.org/10.1111/ggr.12265.

Geisler, T., A. A. Rashwan, M. K. W. Rahn, et al. 2003. "Low-Temperature Hydrothermal Alteration of Natural Metamict Zircons From the Eastern Desert, Egypt." *Mineralogical Magazine* 67: 485–508. https://doi.org/10.1180/0026461036730112.

Geisler, T., U. Schaltegger, and F. Tomaschek. 2007. "Re-Equilibration of Zircon in Aqueous Fluids and Melts." *Elements* 3: 43–50. https://doi.org/10.2113/gselements.3.1.43.

Godinho, J. R. A., S. Piazolo, and T. Balic-Zunic. 2014. "Importance of Surface Structure on Dissolution of Fluorite: Implications for Surface Dynamics and Dissolution Rates." *Geochimica et Cosmochimica Acta* 126: 398–410. https://doi.org/10.1016/J.GCA.2013.11.017.

Halpin, J. A., N. R. Daczko, N. G. Direen, J. A. Mulder, R. C. Murphy, and T. Ishihara. 2020. "Provenance of Rifted Continental Crust at the Nexus of East Gondwana Breakup." *Lithos* 354–355: 105363. https://doi.org/10.1016/j.lithos.2019.105363.

Halpin, J. A., N. R. Daczko, L. A. Milan, and G. L. Clarke. 2012. "Decoding Near-Concordant U–Pb Zircon Ages Spanning Several Hundred Million Years: Recrystallisation, Metamictisation or Diffusion?" *Contributions*

to Mineralogy and Petrology 163: 67–85. https://doi.org/10.1007/s00410-011-0659-7.

Halpin, J. A., T. Jensen, P. McGoldrick, et al. 2014. "Authigenic Monazite and Detrital Zircon Dating From the Proterozoic Rocky Cape Group, Tasmania: Links to the Belt-Purcell Supergroup, North America." *Precambrian Research* 250: 50–67. https://doi.org/10.1016/J.PRECAMRES.2014.05.025.

Harlov, D. E., R. Anczkiewicz, and D. J. Dunkley. 2023. "Metasomatic Alteration of Zircon at Lower Crustal P-T Conditions Utilizing Alkali- and F-Bearing Fluids: Trace Element Incorporation, Depletion, and Resetting the Zircon Geochronometer." *Geochimica et Cosmochimica Acta* 352: 222–235. https://doi.org/10.1016/J.GCA.2023.05.011.

Harlov, D. E., R. Wirth, and H. J. Förster. 2005. "An Experimental Study of Dissolution-Reprecipitation in Fluorapatite: Fluid Infiltration and the Formation of Monazite." *Contributions to Mineralogy and Petrology* 150: 268–286. https://doi.org/10.1007/s00410-005-0017-8.

Hawkesworth, C. J., and A. I. S. Kemp. 2006. "Using Hafnium and Oxygen Isotopes in Zircons to Unravel the Record of Crustal Evolution." *Chemical Geology* 226: 144–162. https://doi.org/10.1016/j.chemgeo.2005.09.018.

He, X. F., M. Hand, M. Santosh, D. E. Kelsey, L. J. Morrissey, and T. Tsunogae. 2018. "Long-Lived Metamorphic P–T–T Evolution of the Highland Complex, Sri Lanka: Insights From Mafic Granulites." *Precambrian Research* 316: 227–243. https://doi.org/10.1016/j.precamres.2018.08.008.

Jochum, K. P., U. Weis, B. Stoll, et al. 2011. "Determination of Reference Values for NIST SRM 610–617 Glasses Following ISO Guidelines." *Geostandards and Geoanalytical Research* 35: 397–429. https://doi.org/10.1111/J.1751-908X.2011.00120.X.

Kelly, C. J., D. A. Schneider, S. E. Jackson, T. Kalbfleisch, and C. R. McFarlane. 2017. "Insights Into Low- To Moderate-Temperature Recrystallization of Zircon: Unpolished Crystal Depth Profile Techniques and Geochemical Mapping." *Chemical Geology* 449: 82–98. https://doi.org/10.1016/J.CHEMGEO.2016.11.035.

Koehn, D., S. Piazolo, N. E. Beaudoin, et al. 2021. "Relative Rates of Fluid Advection, Elemental Diffusion and Replacement Govern Reaction Front Patterns." *Earth and Planetary Science Letters* 565: 116950. https://doi.org/10.1016/J.EPSL.2021.116950.

Korhonen, F. J., C. Clark, M. Brown, S. Bhattacharya, and R. Taylor. 2013. "How Long-Lived Is Ultrahigh Temperature (UHT) Metamorphism? Constraints From Zircon and Monazite Geochronology in the Eastern Ghats Orogenic Belt, India." *Precambrian Research* 234: 322–350. https://doi.org/10.1016/j.precamres.2012.12.001.

Laurent, A. T., B. Bingen, S. Duchene, M. J. Whitehouse, A. Seydoux-Guillaume, and V. Bosse. 2018. "Decoding a Protracted Zircon Geochronological Record in Ultrahigh Temperature Granulite, and Persistence of Partial Melting in the Crust, Rogaland, Norway." *Contributions to Mineralogy and Petrology* 173: 1–25. https://doi.org/10.1007/S00410-018-1455-4/FIGURES/1.

Lenting, C., T. Geisler, A. Gerdes, E. Kooijman, E. E. Scherer, and A. Zeh. 2010. "The Behavior of the Hf Isotope System in Radiation-Damaged Zircon During Experimental Hydrothermal Alteration." *American Mineralogist* 95: 1343–1348. https://doi.org/10.2138/AM.2010.3521.

Lewerentz, A., D. E. Harlov, A. Scherstén, and M. J. Whitehouse. 2019. "Baddeleyite Formation in Zircon by Ca-Bearing Fluids in Silica-Saturated Systems in Nature and Experiment: Resetting of the U-Pb Geochronometer." *Contributions to Mineralogy and Petrology* 174: 64. https://doi.org/10.1007/s00410-019-1600-8.

Milan, L. A., N. R. Daczko, G. L. Clarke, and A. H. Allibone. 2016. "Complexity of In-Situ Zircon U–Pb–Hf Isotope Systematics During Arc Magma Genesis at the Roots of a Cretaceous Arc, Fiordland, New Zealand." *Lithos* 264: 296–314. https://doi.org/10.1016/J.LITHOS.2016.08.023.

Moller, A., P. J. O'Brien, A. Kennedy, and A. Kroner. 2003. "Linking Growth Episodes of Zircon and Metamorphic Textures to Zircon Chemistry: An Example From Ultrahigh-Temperature Granulites of Rogaland (SW Norway)." *Geological Society, London, Special Publications* 220: 65–81. https://doi.org/10.1144/GSL.SP.2003.220.01.04.

Montalvo, P. E., A. J. Cavosie, C. L. Kirkland, et al. 2019. "Detrital Shocked Zircon Provides First Radiometric Age Constraint (<1472 Ma) for the Santa Fe Impact Structure, New Mexico, USA." *GSA Bulletin* 131, no. 5–6: 845–863. https://doi.org/10.1130/B31761.1.

Norberg, N., G. Neusser, R. Wirth, and D. Harlov. 2011. "Microstructural Evolution During Experimental Albitization of K-Rich Alkali Feldspar." *Contributions to Mineralogy and Petrology* 162: 531–546. https://doi.org/10.1007/s00410-011-0610-y.

Norris, A., and L. Danyushevsky. 2018. *Towards Estimating the Complete Uncertainty Budget of Quantified Results Measured by LA-ICP-MS*. Boston: Goldschmidt.

Piazolo, S., H. Austrheim, and M. Whitehouse. 2012. "Brittle-Ductile Microfabrics in Naturally Deformed Zircon: Deformation Mechanisms and Consequences for U-Pb Dating." *American Mineralogist* 97: 1544–1563. https://doi.org/10.2138/am.2012.3966.

Putnis, A. 2009. "Mineral Replacement Reactions." *Reviews in Mineralogy and Geochemistry* 70: 87–124. https://doi.org/10.2138/rmg.2009.70.3.

Putnis, A., and T. John. 2010. "Replacement Processes in the Earth's Crust." *Elements* 6: 159–164. https://doi.org/10.2113/gselements.6.3.159.

Putnis, C. V., and K. Mezger. 2004. "A Mechanism of Mineral Replacement: Isotope Tracing in the Model System KCl-KBr-H_2O." *Geochimica et Cosmochimica Acta* 68: 2839–2848. https://doi.org/10.1016/J.GCA.2003.12.009.

Putnis, C. V., K. Tsukamoto, and Y. Nishimura. 2005. "Direct Observations of Pseudomorphism: Compositional and Textural Evolution at a Fluid-Solid Interface." *American Mineralogist* 90: 1909–1912. https://doi.org/10.2138/am.2005.1990.

Reiners, P. W. 2005. "Zircon (U-TH)/He Thermochronometry." *Reviews in Mineralogy and Geochemistry* 58: 151–179. https://doi.org/10.2138/rmg.2005.58.6.

Rimša, A., M. J. Whitehouse, L. Johansson, and S. Piazolo. 2007. "Brittle Fracturing and Fracture Healing of Zircon: An Integrated Cathodoluminescence, EBSD, U-Th-Pb, and REE Study." *American Mineralogist* 92, no. 7: 1213–1224. https://doi.org/10.2138/am.2007.2458.

Ruiz-Agudo, E., C. V. Putnis, and A. Putnis. 2014. "Coupled Dissolution and Precipitation at Mineral–Fluid Interfaces." *Chemical Geology* 383: 132–146. https://doi.org/10.1016/j.chemgeo.2014.06.007.

Scherer, E., M. Whitehouse, and C. Munker. 2007. "Zircon as a Monitor of Crustal Growth." *Elements* 3: 19–24. https://doi.org/10.2113/gselements.3.1.19.

Schwartz, J. J., B. E. John, M. J. Cheadle, et al. 2010. "Dissolution–Reprecipitation of Igneous Zircon in Mid-Ocean Ridge Gabbro, Atlantis Bank, Southwest Indian Ridge." *Chemical Geology* 274, no. 1–2: 68–81. https://doi.org/10.1016/j.chemgeo.2010.03.017.

Seydoux-Guillaume, A.-M., B. Bingen, V. Bosse, et al. 2018. "Transmission Electron Microscope Imaging Sharpens Geochronological Interpretation of Zircon and Monazite." In *Microstructural Geochronology; Lattice to Atom-Scale Records of Planetary History, AGU Book*. New Jersey, USA: Geophysical Monograph Series. https://doi.org/10.1002/9781119227250.ch12ï.

Simon, H. L., N. M. Kelly, and A. Moller. 2007. "Zircon Behaviour and the Thermal Histories of Mountain Chains." *Elements* 3: 25–30. https://doi.org/10.2113/gselements.3.1.25.

Sláma, J., J. Košler, D. J. Condon, et al. 2008. "Plešovice Zircon — A New Natural Reference Material for U–Pb and Hf Isotopic Microanalysis." *Chemical Geology* 249: 1–35. https://doi.org/10.1016/J.CHEMGEO.2007.11.005.

Spier, C. A., N. R. Daczko, and R. Zhou. 2024. "Zircon Coupled Dissolution-Precipitation Textures Distinguish Xenocrystic Cargo From Rare Magmatic Zircon in the Paleoarchean Bacuri Mafic-Ultramafic Layered Complex, Brazil." *Precambrian Research* 404: 107342. https://doi.org/10.1016/J.PRECAMRES.2024.107342.

Spier, C. A., C. F. F. Filho, and N. Daczko. 2022. "Zircon U-Pb Isotopic and Geochemical Study of Metanorites From the Chromite-Mineralised Bacuri Mafic-Ultramafic Complex: Insights of a Paleoarchean Crust in the Amapá Block, Guyana Shield, Brazil." *Gondwana Research* 105: 262–289. https://doi.org/10.1016/J.GR.2021.09.010.

Spruzeniece, L., S. Piazolo, and H. E. Maynard-Casely. 2017. "Deformation-Resembling Microstructure Created by Fluid-Mediated Dissolution-Precipitation Reactions." *Nature Communications* 8: 1–9. https://doi.org/10.1038/ncomms14032.

Szymczak, P., and A. J. C. Ladd. 2014. "Reactive-Infiltration Instabilities in Rocks. Part 2. Dissolution of a Porous Matrix." *Journal of Fluid Mechanics* 738: 591–630. https://doi.org/10.1017/jfm.2013.586.

Taylor, R. J., S. M. Reddy, D. W. Saxey, et al. 2023. "Direct age Constraints on the Magnetism of Jack Hills Zircon. Science." *Advances* 9, no. 1: eadd1511. https://doi.org/10.1126/sciadv.add1511.

Thompson, J., S. Meffre, and L. Danyushevsky. 2018. "Impact of Air, Laser Pulse Width and Fluence on U–Pb Dating of Zircons by LA-ICPMS." *Journal of Analytical Atomic Spectrometry* 33: 221–230. https://doi.org/10.1039/C7JA00357A.

Valley, J. W. 2003. "Oxygen Isotopes in Zircon." *Reviews in Mineralogy and Geochemistry* 1: 343–385. https://doi.org/10.2113/0530343.

Varga, J., T. Raimondo, N. R. Daczko, and J. Adam. 2020. "Experimental Alteration of Monazite in Granitic Melt: Variable U–Th–Pb and REE Mobility During Melt-Mediated Coupled Dissolution-Precipitation." *Chemical Geology* 544: 119602. https://doi.org/10.1016/j.chemgeo.2020.119602.

Vermeesch, P. 2018. "IsoplotR: A Free and Open Toolbox for Geochronology." *Geoscience Frontiers* 9, no. 5: 1479–1493. https://doi.org/10.1016/j.gsf.2018.04.001.

Vonlanthen, P., J. D. F. Gerald, D. Rubatto, and J. Hermann. 2012. "Recrystallization Rims in Zircon (Valle d'Arbedo, Switzerland): An Integrated Cathodoluminescence, LA-ICP-MS, SHRIMP, and TEM Study." *American Mineralogist* 97: 369–377. https://doi.org/10.2138/am.2012.3854.

Wang, Y., P. Gao, G. C. Sun, et al. 2024. "Zircon Hf Isotope Behaviour During the Magmatic-Hydrothermal Processes: A Case Study From the Yashan Pluton, South China." *Lithos* 470–471: 107519. https://doi.org/10.1016/j.lithos.2024.107519.

Wiedenbeck, M., P. Alle, F. Corfu, et al. 1995. "Three Natural Zircon Standards for U-Th-Pb, Lu-Hf, Trace Element and REE Analyses." *Geostandards Newsletter* 19: 1–23. https://doi.org/10.1111/J.1751-908X.1995.TB00147.X.

Yin, A., C. S. Dubey, A. A. G. Webb, et al. 2010. "Geologic Correlation of the Himalayan Orogen and Indian Craton: Part 1. Structural Geology, U-Pb Zircon Geochronology, and Tectonic Evolution of the Shillong Plateau and Its Neighboring Regions in NE India." *Bulletin of the Geological Society of America* 122: 336–359. https://doi.org/10.1130/B26460.1.

Zhong, S., C. Feng, R. Seltmann, D. Li, and H. Qu. 2018. "Can Magmatic Zircon Be Distinguished From Hydrothermal Zircon by Trace Element Composition? The Effect of Mineral Inclusions on Zircon Trace Element Composition." *Lithos* 314: 646–657. https://doi.org/10.1016/j.lithos.2018.06.029.

Supporting Information

Additional supporting information can be found online in the Supporting Information section.